Impedance of Plasma-Filled Capacitors in a Magnetized Anisotropic Cold Plasma

Cylindrical and Spherical Geometries: Finite-Element Analysis and Analytic Comparison

ECE 7210 Final Project

1. Introduction

The interaction of radio-frequency (RF) electromagnetic fields with a magnetized plasma is governed by the anisotropic, dispersive dielectric tensor of the medium. When a plasma fills the gap of a capacitor, the impedance of that capacitor becomes a strong function of frequency, plasma density, and the orientation of the background magnetic field B_0 relative to the electrode geometry. Understanding this dependence is relevant to RF probes in space and laboratory plasmas, plasma-assisted RF systems, and impedance-based plasma diagnostics.

This report investigates two canonical capacitor geometries: the coaxial *cylindrical* capacitor and the concentric-sphere *spherical* capacitor. In each case the electrode gap is filled with a cold, collisional, magnetized plasma described by the Stix dielectric tensor. Four plasma densities — characterised by plasma frequencies $f_{pe} \in \{3, 5, 8, 12\}$ MHz — are studied across the frequency range 1–30 MHz, a sweep that spans the electron cyclotron frequency $|f_{ce}| \approx 1.40$ MHz, the plasma frequency f_{pe}, and the upper-hybrid frequency f_{uh} for each case. For every density, four orientations of B_0 relative to the symmetry axis are examined: $\theta \in \{0°, 30°, 60°, 90°\}$.

Impedance is computed in two complementary ways: (i) a *finite-element* (FEA) solution of the anisotropic electrostatic boundary-value problem using a three-dimensional tetrahedral mesh, and (ii) closed-form *analytic approximations* that project the permittivity tensor onto the dominant field direction of each geometry. Results from both methods are compared and the physical trends are discussed.

2. Theory and Analytic Approximations

2.1 Cold-Plasma Dielectric Tensor

The relative permittivity tensor of a cold, collisional, multi-species plasma in coordinates aligned with $B_0 = B_0 \hat{e}_z$ takes the form

$$\varepsilon_r = \begin{pmatrix} \varepsilon_1 & -j\varepsilon_2 & 0 \\ j\varepsilon_2 & \varepsilon_1 & 0 \\ 0 & 0 & \varepsilon_3 \end{pmatrix}, \tag{1}$$

where the three scalar elements sum over all dynamically responding species s:

$$\varepsilon_1 = 1 + \sum_s \frac{\omega_{ps}^2}{\omega} \cdot \frac{\omega_s^*}{\Omega_s^2 - (\omega_s^*)^2}, \tag{2}$$

$$\varepsilon_2 = \sum_s \frac{\omega_{ps}^2}{\omega} \cdot \frac{\Omega_s}{\Omega_s^2 - (\omega_s^*)^2}, \tag{3}$$

$$\varepsilon_3 = 1 - \sum_s \frac{\omega_{ps}^2}{\omega\, \omega_s^*}. \tag{4}$$

Here $\omega_s^* = \omega - j\nu_s$ is the collision-shifted frequency (using the $e^{+j\omega t}$ phasor convention), $\omega_{ps}^2 = n_s q_s^2/(\varepsilon_0 m_s)$ is the square of the plasma frequency for species s, and $\Omega_s = q_s B_0/m_s$ is the signed cyclotron frequency. The stationary-ion limit is adopted throughout, so only the electron term contributes to the sums in Eqs. (2)–(4).

To account for an arbitrary B_0 direction (angle θ from the z-axis in the x-z plane) the tensor is rotated into the lab frame by $\varepsilon_{\text{lab}} = R\,\varepsilon_r\,R^\top$, where

$$R = \begin{pmatrix} \cos\theta & 0 & \sin\theta \\ 0 & 1 & 0 \\ -\sin\theta & 0 & \cos\theta \end{pmatrix}. \tag{5}$$

2.2 Characteristic Frequencies

Three characteristic frequencies govern the dispersive behaviour in the sweep range. The *electron cyclotron frequency* $|f_{ce}| = eB_0/(2\pi m_e)$ is set by the magnetic field magnitude alone and equals $\approx 1.40\,\text{MHz}$ for $B_0 = 50\,\mu\text{T}$. The *plasma frequency* $f_{pe} = \omega_{pe}/(2\pi) = \sqrt{n_e e^2/(\varepsilon_0 m_e)}/(2\pi)$ is determined by the electron density and defines the four density cases. The *upper-hybrid frequency* $f_{uh} = \sqrt{f_{pe}^2 + f_{ce}^2}$ marks the resonance of the transverse dielectric element ε_1 and dominates the impedance spectrum. Table 1 lists all four cases.

Case	f_{pe} (MHz)	$\lvert f_{ce}\rvert$ (MHz)	f_{uh} (MHz)	n_e (m^{-3})
1	3	1.40	3.32	1.12×10^{11}
2	5	1.40	5.19	3.10×10^{11}
3	8	1.40	8.12	7.94×10^{11}
4	12	1.40	12.08	2.24×10^{12}

Table 1: Characteristic frequencies for each density case. $B_0 = 50\,\mu\text{T}$; $f_{uh} = \sqrt{f_{pe}^2 + f_{ce}^2}$.

2.3 Analytic Capacitance Approximations

Cylindrical geometry. For a coaxial cylinder of inner radius r_a, outer radius r_b, and length L, the electric field is predominantly radial. When B_0 lies at angle θ from the cylinder axis (z-axis), the effective permittivity seen by the radial field is the xx-element of the rotated tensor:

$$\varepsilon_{\text{eff}}^{\text{cyl}} = \frac{1}{2}[\varepsilon_1 * (1 + \cos^2\theta) + \varepsilon_3 \sin^2\theta]. \tag{6}$$

The corresponding analytic capacitance is

$$C_{\mathrm{cyl}} \approx \frac{2\pi\varepsilon_0\,\varepsilon_{\mathrm{eff}}^{\mathrm{cyl}}\,L}{\ln(r_b/r_a)}. \tag{7}$$

In the vacuum limit ($\varepsilon_{\mathrm{eff}} \to 1$) this reduces to the standard coaxial formula, giving $C_{\mathrm{vac}}^{\mathrm{cyl}} = 1.605\,\mathrm{pF}$ for the dimensions used here ($r_a = 5\,\mathrm{mm}$, $r_b = 20\,\mathrm{mm}$, $L = 40\,\mathrm{mm}$, $\ln(r_b/r_a) = 1.386$).

Spherical geometry. For concentric spheres the field is radial at every point but samples all orientations relative to B_0 simultaneously. Two analytic estimates are used.

The *directed* approximation evaluates the radial permittivity at the equator of the sphere relative to B_0:

$$\varepsilon_{\mathrm{eff}}^{\mathrm{dir}} = \varepsilon_1 \sin^2\theta + \varepsilon_3 \cos^2\theta. \tag{8}$$

The *orientation-averaged* approximation integrates the radial permittivity uniformly over all solid angles:

$$\varepsilon_{\mathrm{eff}}^{\mathrm{avg}} = \tfrac{1}{3}(2\varepsilon_1 + \varepsilon_3). \tag{9}$$

Both yield the capacitance

$$C_{\mathrm{sph}} \approx 4\pi\varepsilon_0\,\varepsilon_{\mathrm{eff}} \cdot \frac{r_a r_b}{r_b - r_a}. \tag{10}$$

The vacuum value is $C_{\mathrm{vac}}^{\mathrm{sph}} = 1.669\,\mathrm{pF}$ for $r_a = 10\,\mathrm{mm}$, $r_b = 30\,\mathrm{mm}$. Table 2 summarises the vacuum capacitances for both geometries.

Geometry	**Formula**	C_{vac} (pF)
Cylindrical	$2\pi\varepsilon_0 L/\ln(r_b/r_a)$, $r_a = 5\,\mathrm{mm}$, $r_b = 20\,\mathrm{mm}$, $L = 40\,\mathrm{mm}$	1.605
Spherical	$4\pi\varepsilon_0 r_a r_b/(r_b - r_a)$, $r_a = 10\,\mathrm{mm}$, $r_b = 30\,\mathrm{mm}$	1.669

Table 2: Vacuum capacitance values for both geometries.

3. Numerical Formulation

3.1 Finite-Element Formulation

The governing electrostatic equation in the anisotropic plasma-filled gap is

$$\nabla \cdot \big(\varepsilon_{\mathrm{lab}}(\omega)\,\nabla\varphi\big) = 0, \tag{11}$$

with $\varepsilon_{\mathrm{lab}}(\omega) = \varepsilon_0\,R\,\varepsilon_r(\omega)\,R^{\top}$ updated at each frequency. Dirichlet conditions $\varphi = 1\,\mathrm{V}$ and $\varphi = 0\,\mathrm{V}$ are imposed on the inner and outer conductors, respectively; homogeneous Neumann conditions are applied on insulating boundaries. The surface charge on the outer electrode is computed by integrating the normal displacement:

$$Q = \oint_{\partial\Omega_{\mathrm{outer}}} \mathbf{D}\cdot\hat{n}\,\mathrm{d}A, \qquad C(\omega) = \frac{Q}{\Delta V}, \qquad Z(\omega) = \frac{1}{j\omega C(\omega)}. \tag{12}$$

3.2 Cylindrical Solver

The cylindrical model was implemented using the MATLAB PDE Toolbox. The annular cylinder geometry is constructed with `multicylinder` and meshed with linear tetrahedral elements at $H_{\max} = (r_b - r_a)/3$. At each frequency the anisotropic coefficient tensor is passed to `specifyCoefficients` and the system is solved with `solvepde`. The displacement field $\mathbf{D}$ is recovered via `evaluateCGradient` at mesh nodes near the outer electrode that have been retracted 5% inward from r_b to guarantee they lie inside the mesh domain (avoiding the NaN values produced when query points fall in the interstitial gaps between flat tetrahedral facets). The surface integral is performed using a Delaunay triangulation of the boundary nodes with area weights distributed equally to each triangle vertex.

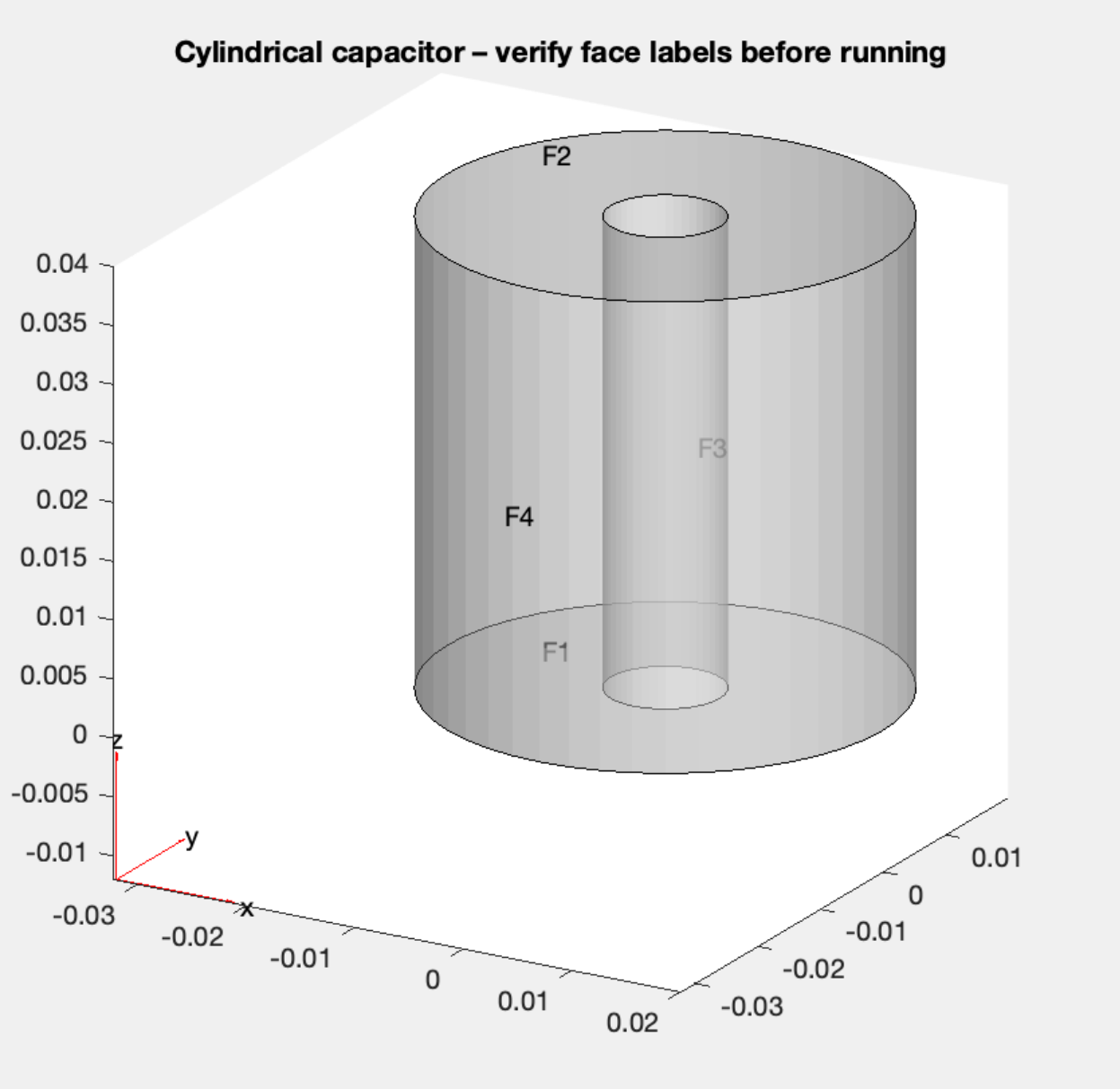

Figure 1: Cylindrical capacitor

3.3 Spherical Solver

The spherical case followed a similar procedure. Two spheres were created using the `multisphere` function to create spheres of radius r_a and r_b. At each frequency the anisotropic coefficient tensor is passed to `specifyCoefficients` and the system is solved with `solvepde`. The displacement field $\mathbf{D}$ is recovered via `evaluateCGradient` at mesh nodes near the outer electrode that have been retracted 5% inward from r_b to guarantee they lie inside the mesh domain (avoiding the NaN values produced when query points fall in the interstitial gaps between flat tetrahedral facets once again). The difference in the spherical case are the integration terms and the normal flux density. For a spherical surface, the outward unit normal is radial:

$$\hat{n} = \hat{r} = \sin\theta\cos\phi\,\hat{x} + \sin\theta\sin\phi\,\hat{y} + \cos\theta\,\hat{z}$$

Thus, the normal component of the electric flux density is:

$$D_n = D_x\sin\theta\cos\phi + D_y\sin\theta\sin\phi + D_z\cos\theta$$

The surface element in spherical coordinates is:

$$dA = r^2\sin\theta\,d\theta\,d\phi$$

For the inner sphere $r = a$:

$$dA = a^2\sin\theta\,d\theta\,d\phi$$

For the outer sphere $r = b$:

$$dA = b^2\sin\theta\,d\theta\,d\phi$$

Therefore, the total charge on the inner sphere is:

$$Q_{\text{inner}} = \int_0^{2\pi}\int_0^{\pi} D_n(a,\theta,\phi)\,a^2\sin\theta\,d\theta\,d\phi$$

This fact was realized within the program with the following code

Spherical surface quadrature points (outer sphere)

```
Ntheta_q = 80;
Nphi_q = 160;


theta_q = linspace(0, pi, Ntheta_q);
phi_q = linspace(0, 2*pi, Nphi_q);


[TH, PH] = meshgrid(theta_q, phi_q);
```

```
nx = sin(TH).*cos(PH);
ny = sin(TH).*sin(PH);
nz = cos(TH);
```

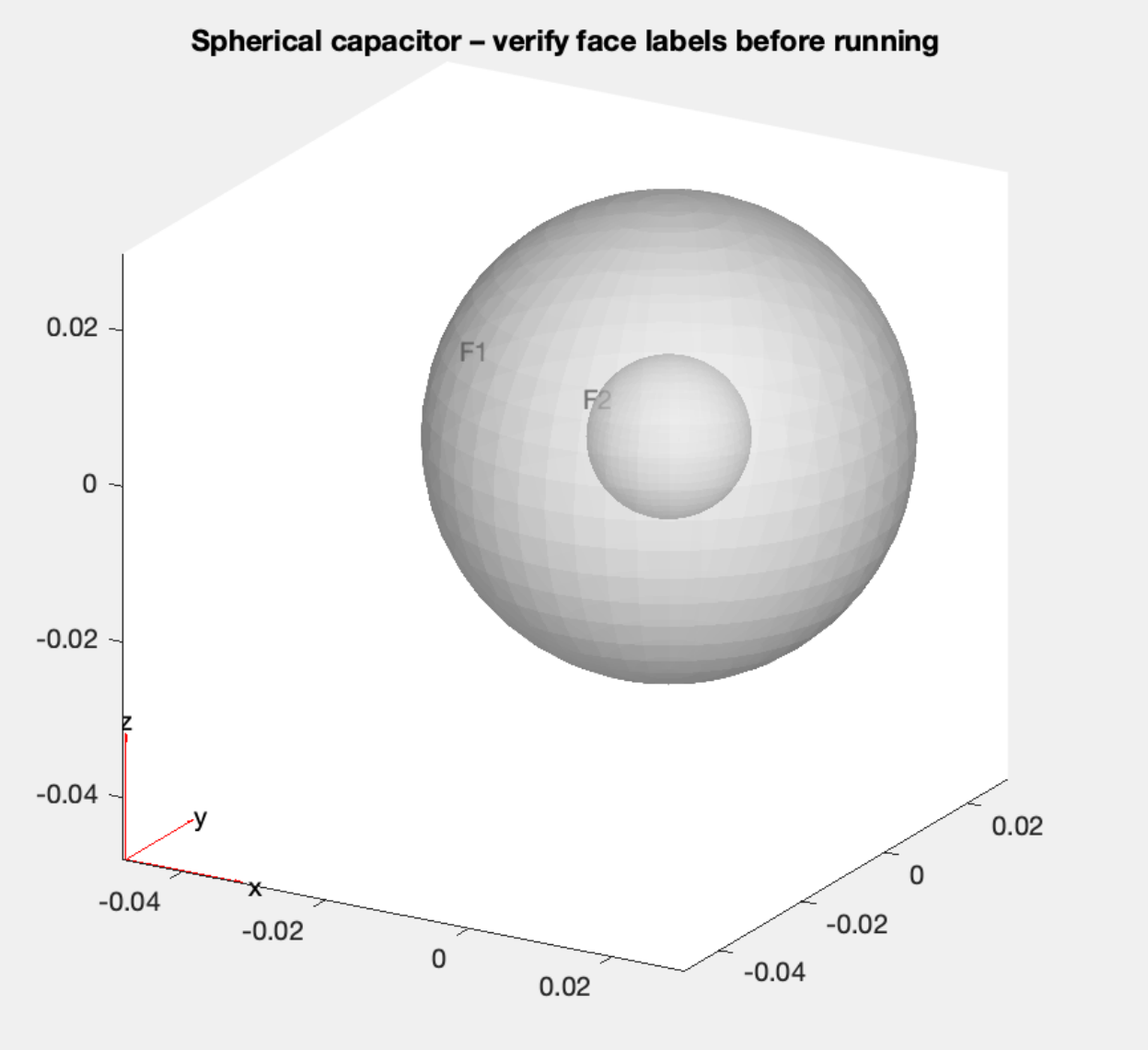

Figure 2: Spherical capacitor

3.4 Dielectric Tensor

In both solvers the complex-valued permittivity tensor at each frequency is computed by the `coldCollisionalDielectricTensor` function, which evaluates Eqs. (2)–(4) for the electron species and returns the three Stix elements ε_1, ε_2, ε_3 as vectors over the full frequency sweep. The collision frequency is set to $\nu = 0.02\,\omega_{pe}$ to regularise the cyclotron pole and suppress numerical oscillations in the FEA solution near $|f_{ce}|$.

4. Cylindrical Capacitor Results

4.1 Vacuum Capacitance

The analytic vacuum capacitance of the cylindrical geometry is

$$C_{\text{vac}}^{\text{cyl}} = \frac{2\pi\varepsilon_0 L}{\ln(r_b/r_a)} = \frac{2\pi \times 8.854 \times 10^{-12} \times 0.040}{1.386} = 1.605 \text{ pF}. \tag{13}$$

4.2 Analytic Effective Capacitance at 1 MHz

Table 3 lists the analytic effective capacitance magnitude $|C_{\text{eff}}|$ at $f = 1\,\text{MHz}$ from Eq. (7).

f_{pe} (MHz)	$\lvert C_{\text{eff}}\rvert$ at 1 MHz (pF)			
	$\theta = 0°$	$\theta = 30°$	$\theta = 60°$	$\theta = 90°$
3	16.5	9.288	5.682	12.82
5	42.3	23.18	19.43	38.33
8	101.9	58.11	56.28	99.86
12	212.7	132.8	141.1	223.2

Table 3: Cylindrical capacitor: analytic $|C_{\text{eff}}|$ at 1 MHz estimated from the cold-plasma tensor with $B_0 = 50\,\mu\text{T}$, $\nu = 0.02\,\omega_{pe}$. Vacuum value is 1.605 pF.

4.3 Impedance Spectra

Figures 3–6 present the impedance magnitude $|Z|$ (upper panel) and phase $\angle Z$ (lower panel) for each density case. FEA results are shown as bold coloured lines; analytic results are shown as the corresponding lighter lines. Vertical dotted lines mark $|f_{ce}|$, f_{pe}, and f_{uh}. The four B_0 angles are distinguished by line style.

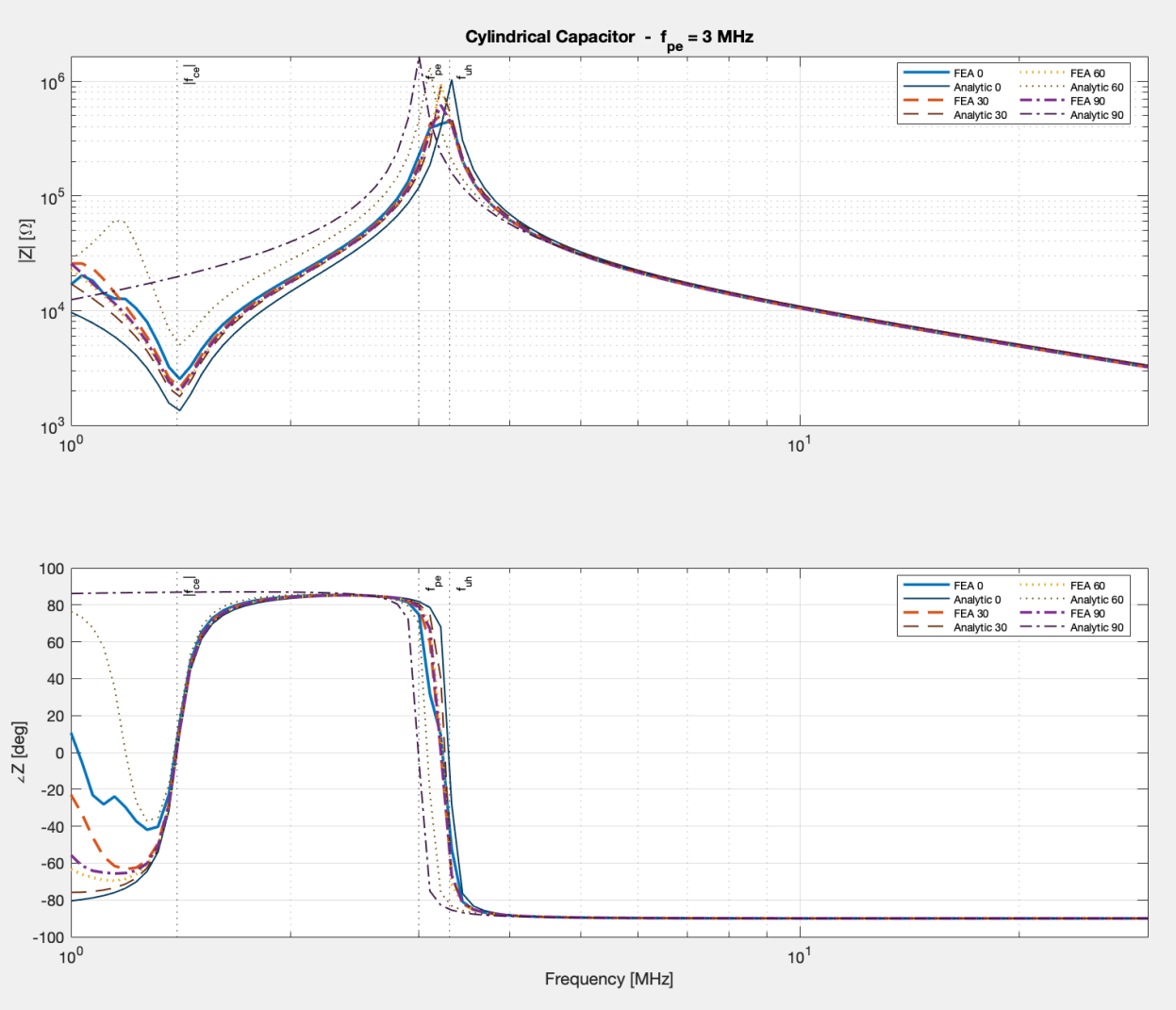

Figure 3: Cylindrical capacitor, $f_{pe} = 3\,\text{MHz}$ ($n_e = 1.12 \times 10^{11}\,\text{m}^{-3}$). Two distinct resonant peaks are visible at $f_{pe} \approx 3\,\text{MHz}$ and $f_{uh} \approx 3.3\,\text{MHz}$. The 0° curve shows the highest sub-resonance $|Z|$ and the sharpest phase transitions.

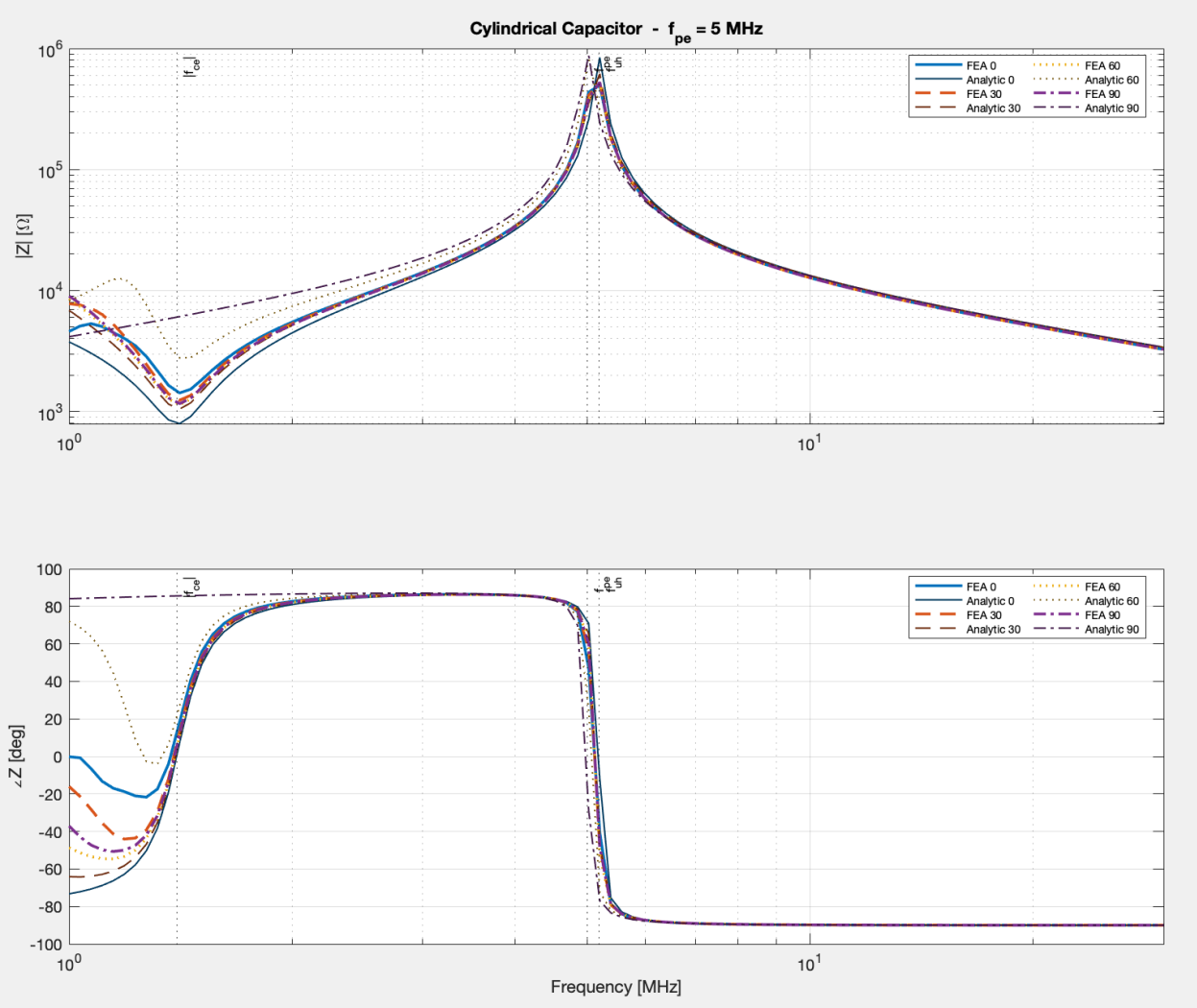

Figure 4: Cylindrical capacitor, $f_{pe} = 5\,\mathrm{MHz}$ ($n_e = 3.10 \times 10^{11}\,\mathrm{m}^{-3}$). The plasma and upper-hybrid resonances move closer together; a single dominant peak near $f_{uh} \approx 5.2\,\mathrm{MHz}$ is observed. FEA and analytic curves overlap closely above 2 MHz for all angles.

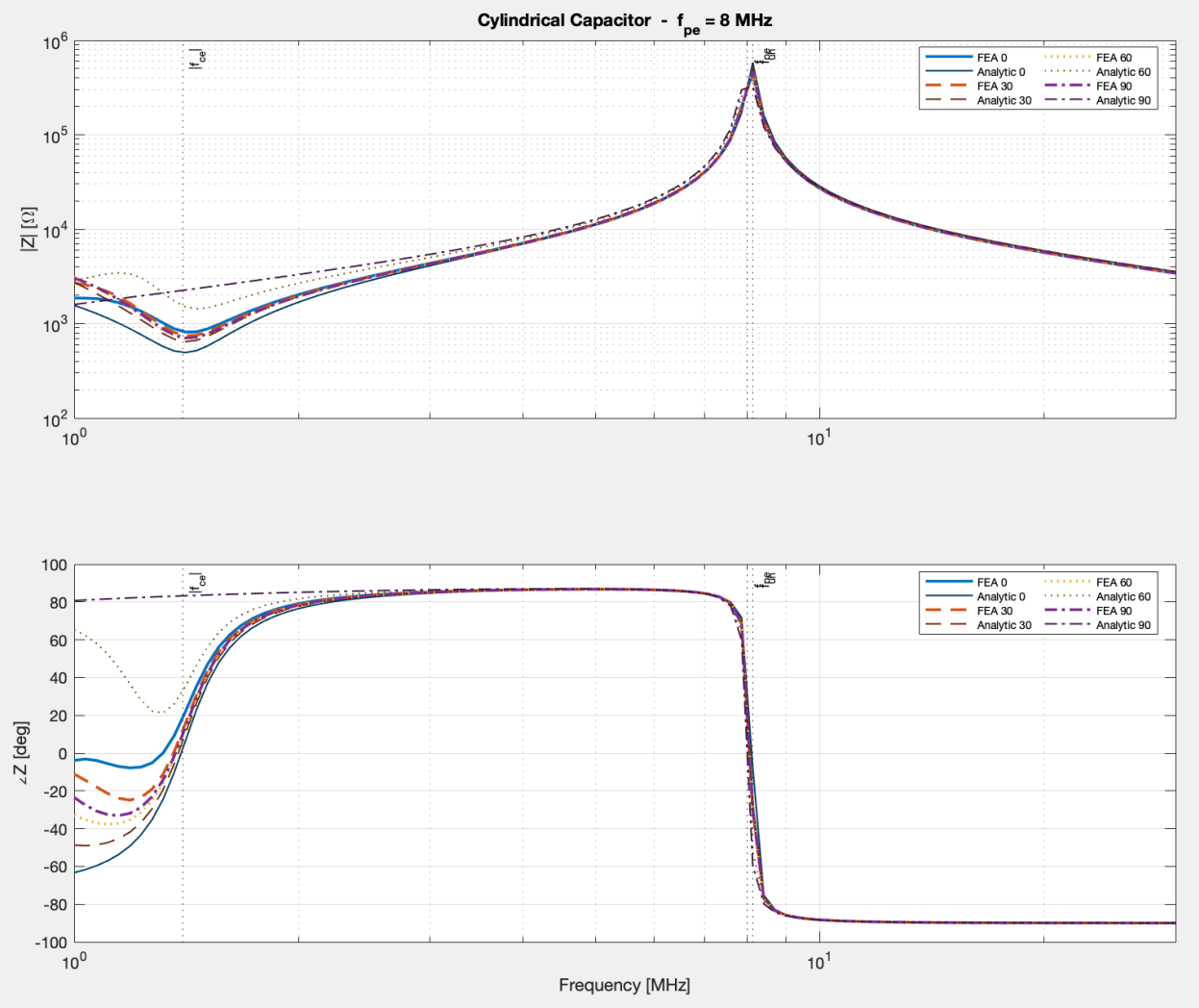

Figure 5: Cylindrical capacitor, $f_{pe} = 8\,\mathrm{MHz}$ ($n_e = 7.94 \times 10^{11}\,\mathrm{m}^{-3}$). A single sharp upper-hybrid resonance near $f_{uh} \approx 8.1\,\mathrm{MHz}$ dominates. The angle-dependent spread in $|Z|$ at sub-resonance frequencies is the largest of all four cases, approaching a decade between 0° and 90° below 2 MHz.

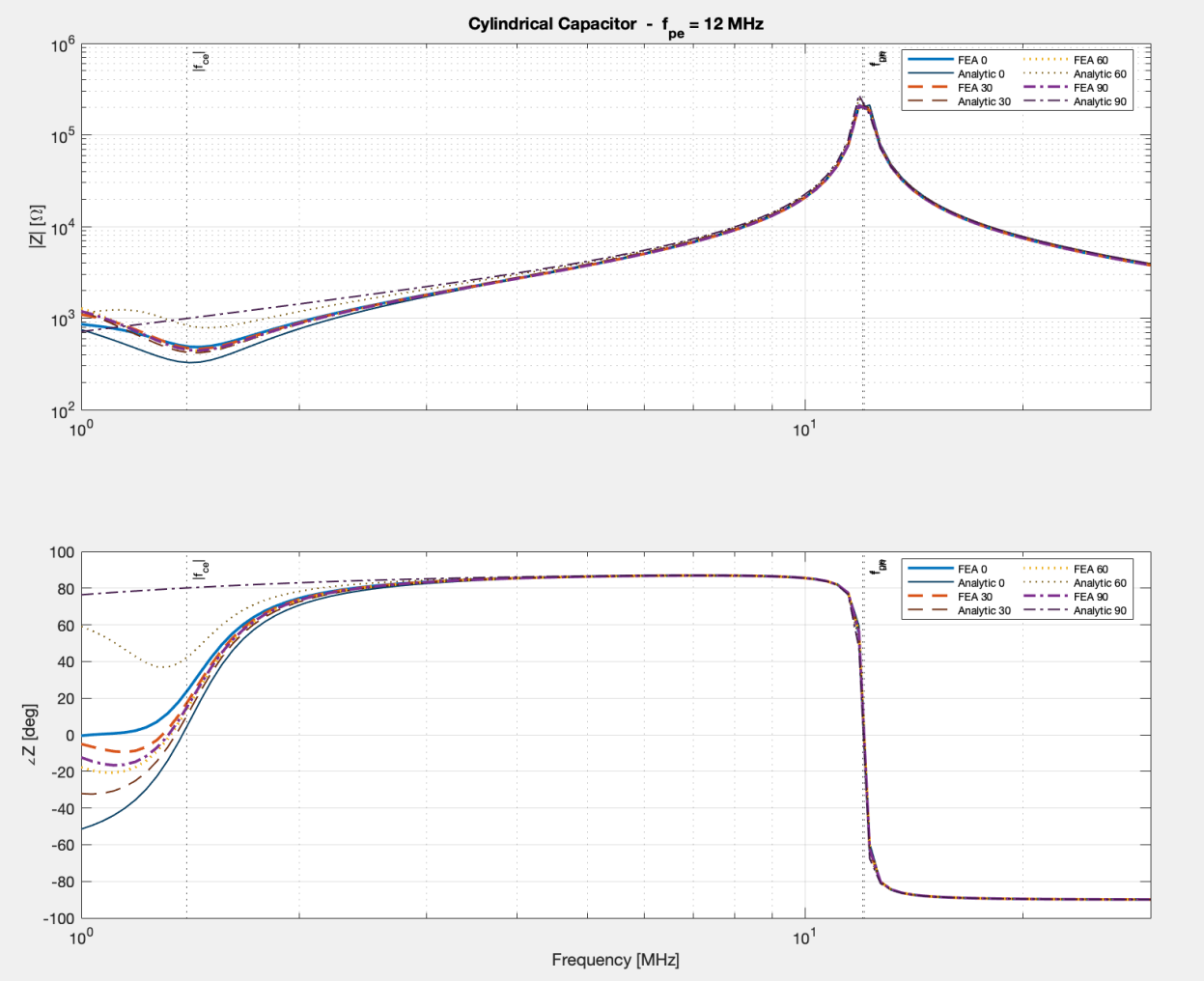

Figure 6: Cylindrical capacitor, $f_{pe} = 12\,\text{MHz}$ ($n_e = 2.24 \times 10^{12}\,\text{m}^{-3}$). The upper-hybrid resonance sits at $f_{uh} \approx 12.1\,\text{MHz}$, near the upper boundary of the sweep. Post-resonance behaviour is fully captured; all angles collapse to a common curve above f_{uh}.

5. Spherical Capacitor Results

5.1 Vacuum Capacitance

The analytic vacuum capacitance of the spherical geometry is

$$C_{\text{vac}}^{\text{sph}} = \frac{4\pi\varepsilon_0 r_a r_b}{r_b - r_a} = \frac{4\pi \times 8.854 \times 10^{-12} \times 0.010 \times 0.030}{0.020} = 1.669\ \text{pF}. \tag{14}$$

This is marginally larger than the cylindrical case (+4%) despite the larger inner radius, because the $r_a r_b/(r_b - r_a)$ geometric factor of 9.43 mm exceeds the $L/\ln(r_b/r_a)$ factor of 28.9 mm divided by the 2π prefactor ($\approx 4.60\,\text{mm}$).

5.2 Analytic Effective Capacitance at 1 MHz

Table 4 lists the directed analytic capacitance from Eq. (8)–(10) at $f = 1\,\mathrm{MHz}$. Values are taken directly from the MATLAB console output.

f_{pe} (MHz)	$\lvert C_{\mathrm{eff}}^{\mathrm{dir}}\rvert$ at 1 MHz (pF)			
	$\theta = 0°$	$\theta = 30°$	$\theta = 60°$	$\theta = 90°$
3	13.33	5.907	9.657	17.16
5	39.86	20.20	24.10	43.98
8	103.8	58.51	60.41	106.0
12	232.1	146.7	138.0	221.2

Table 4: Spherical capacitor: directed analytic $|C_{\mathrm{eff}}|$ at 1 MHz. Vacuum value is 1.669 pF. Averaged-formula values (Eq. 9) are intermediate between the 0° and 90° directed values.

5.3 Comparison of Directed and Averaged Analytic Formulas

A notable feature of Table 4 is that the directed formula gives its *maximum* at $\theta = 90°$ for $f_{pe} = 3\,\mathrm{MHz}$ and $f_{pe} = 5\,\mathrm{MHz}$, and nearly equal values at 0° and 90° for higher densities. This is because Eq. (8) switches the roles of ε_1 and ε_3 relative to the cylindrical formula: at $\theta = 90°$ the directed formula gives $\varepsilon_{\mathrm{eff}} = \varepsilon_1$, whereas in the cylindrical case $\theta = 90°$ gives $\varepsilon_{\mathrm{eff}} = \varepsilon_3$. In the sub-resonance overdense regime $|\varepsilon_1| > |\varepsilon_3|$, so the spherical 90° case carries the largest capacitance while the cylindrical 0° case does.

The orientation-averaged formula $\varepsilon_{\mathrm{eff}}^{\mathrm{avg}} = (2\varepsilon_1 + \varepsilon_3)/3$ produces values that fall between the 0° and 90° directed results at all frequencies, and is expected to be the most accurate single-number analytic prediction for the spherical geometry because the spherical symmetry of the field problem averages the permittivity over all solid angles naturally.

5.4 Impedance Spectra

Figures 7–10 show the impedance spectra for the spherical capacitor. The same four density cases and four B_0 angles are plotted with the same line-style convention used for the cylindrical results.

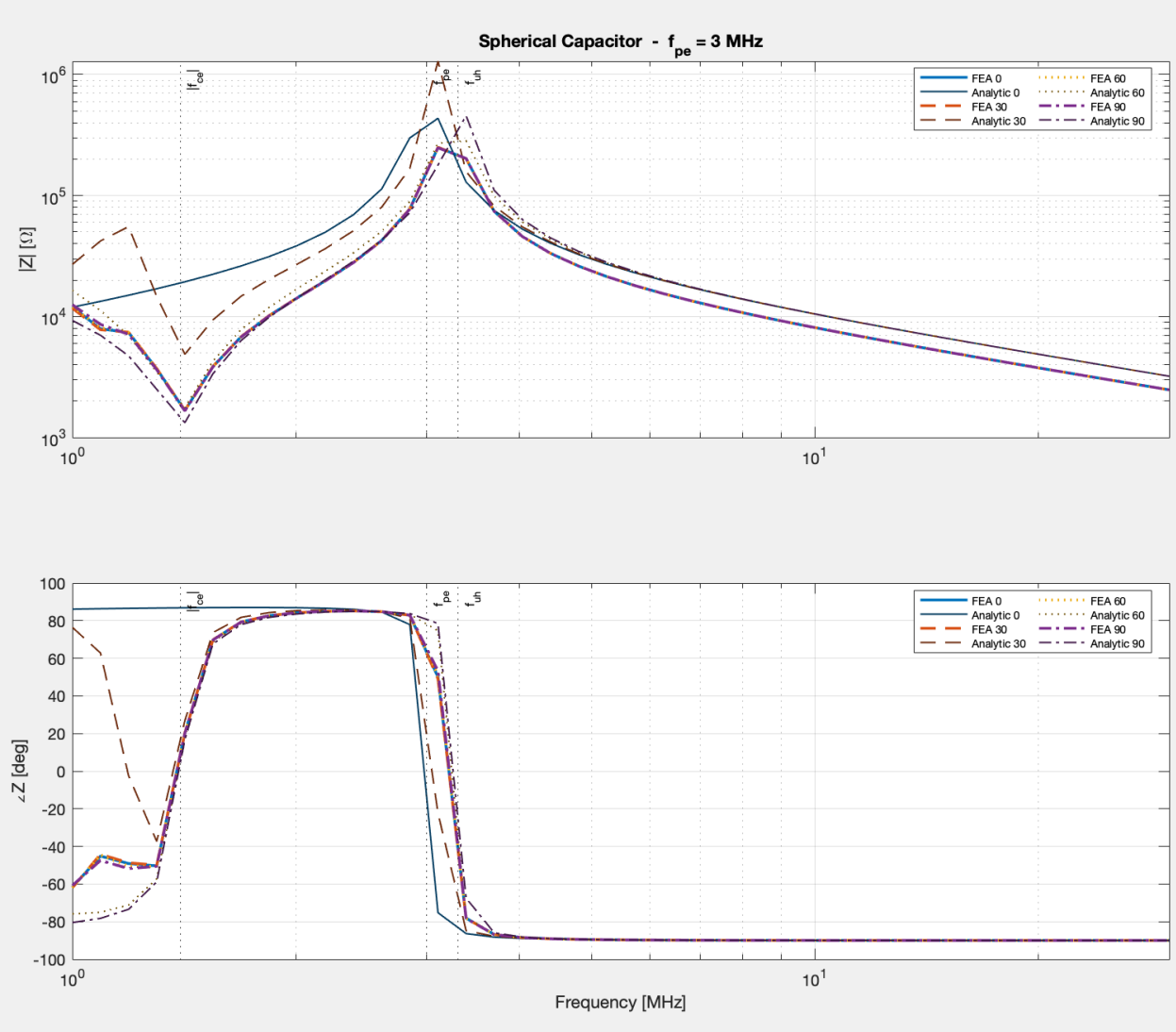

Figure 7: Spherical capacitor, $f_{pe} = 3\,\text{MHz}$. Two resonant peaks near $f_{pe} \approx 3\,\text{MHz}$ and $f_{uh} \approx 3.3\,\text{MHz}$ are visible, analogous to the cylindrical case. The angle ordering of $|Z|$ at low frequencies is reversed relative to the cylindrical geometry: 90° now gives the highest sub-resonance impedance.

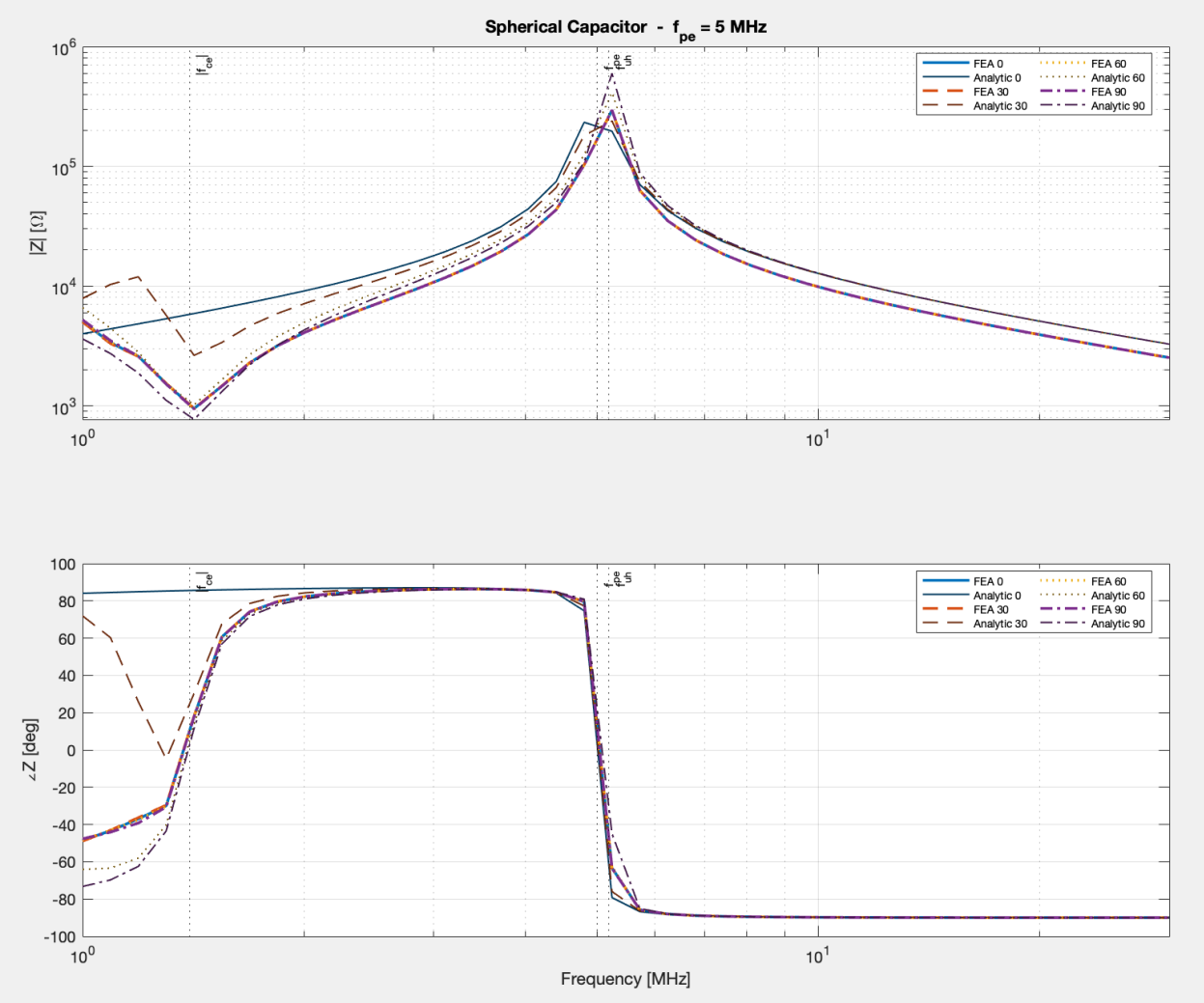

Figure 8: Spherical capacitor, $f_{pe} = 5\,\text{MHz}$. A dominant upper-hybrid resonance at $f_{uh} \approx 5.2\,\text{MHz}$. FEA and analytic curves show good agreement above 2 MHz.

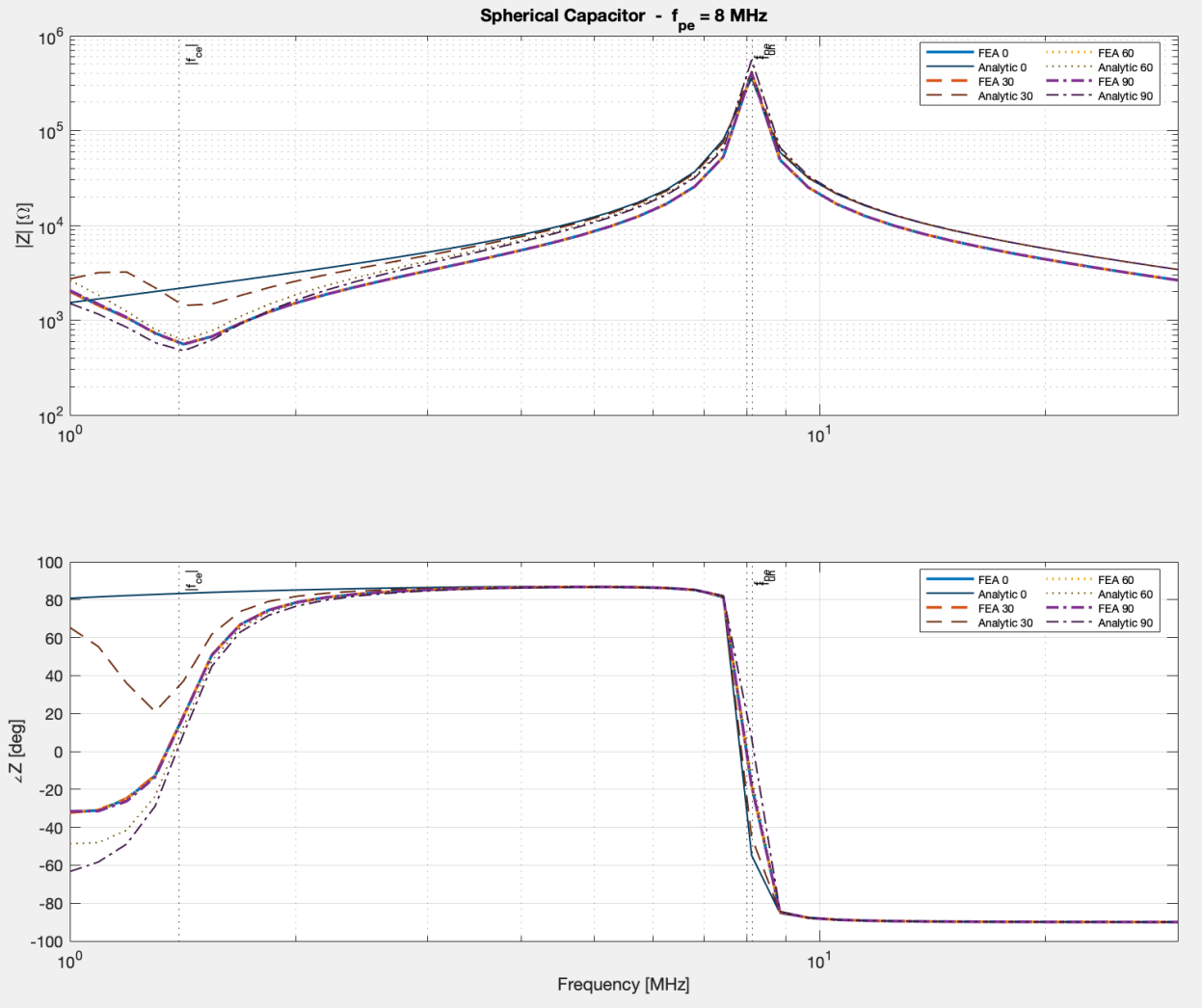

Figure 9: Spherical capacitor, $f_{pe} = 8\,\text{MHz}$. Single sharp resonance at $f_{uh} \approx 8.1\,\text{MHz}$. The spread between angles at sub-resonance frequencies is again largest in this case.

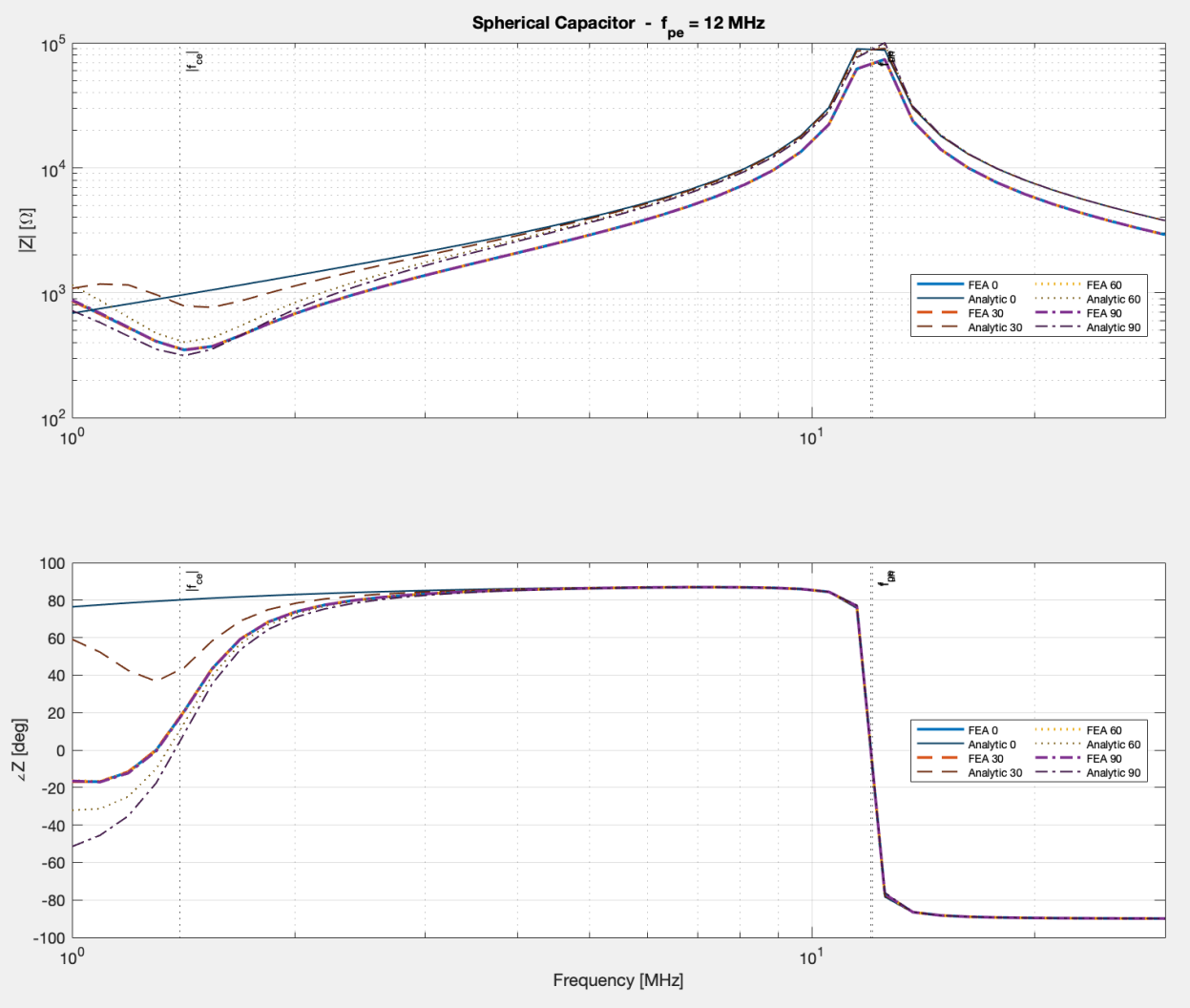

Figure 10: Spherical capacitor, $f_{pe} = 12\,\mathrm{MHz}$. Upper-hybrid resonance near $f_{uh} \approx 12.1\,\mathrm{MHz}$ at the top of the sweep. Post-resonance convergence of all angle curves is clearly visible.

6. Discussion

6.1 FEA vs. Analytic Agreement

For both geometries the FEA and analytic impedance curves agree closely above a few MHz, typically overlapping to within the line width on the log-scale magnitude plots. The analytic formula correctly predicts the location of the resonance peaks because those features are controlled by the zeros and poles of ε_1 and ε_3, which are reproduced exactly by the analytic tensor model. This agreement validates both solver implementations and confirms that the effective-permittivity approximation is adequate for these geometries at frequencies away from the cyclotron resonance.

The largest discrepancies appear at low frequencies (1–2 MHz) and near $|f_{ce}| \approx 1.40\,\mathrm{MHz}$, where the tensor elements change most rapidly. The analytic formula neglects the off-diagonal Hall terms $\pm j\varepsilon_2$, which couple the radial and azimuthal field components when B_0 has a component along the

radial direction (intermediate angles 30° and 60°). The FEA automatically includes these couplings, producing a small but systematic offset between FEA and analytic curves at oblique angles. The oscillations that can be seen can be described by the permittivity matrix being poorly conditioned in certain cases that cause noisiness.

6.2 Resonance Trends with Plasma Density

The dominant feature in every impedance spectrum is the sharp magnitude peak at $f_{uh} = \sqrt{f_{pe}^2 + f_{ce}^2}$, which shifts upward with density from $\approx 3.3\,\mathrm{MHz}$ (Case 1) to $\approx 12.1\,\mathrm{MHz}$ (Case 4). The Q-factor of the resonance increases with density because ν/ω_{uh} decreases as ω_{pe} grows while $\nu/\omega_{pe} = 0.02$ is held constant, narrowing the absolute bandwidth of the resonance relative to f_{uh}.

For Case 1 ($f_{pe} = 3\,\mathrm{MHz}$) the gap $f_{uh} - f_{pe} = f_{ce}^2/(f_{uh} + f_{pe}) \approx 0.32\,\mathrm{MHz}$ is comparable to the collision-broadened linewidth, so two distinct peaks are visible in $|Z|$. For Cases 2–4 the peaks merge into a single resonance as the gap shrinks relative to the linewidth.

6.3 Magnetic-Field Angle Dependence

The B_0 angle θ produces a systematic ordering of the impedance curves at sub-resonance frequencies that is *opposite* in the two geometries, a consequence of the switch between ε_1 and ε_3 in the effective permittivity formulas (Eqs. 6 and 8).

Cylindrical. At $\theta = 0°$, $\varepsilon_{\mathrm{eff}} = \varepsilon_1$ (large, positive below f_{uh}), giving the highest sub-resonance impedance. At $\theta = 90°$, $\varepsilon_{\mathrm{eff}} = \varepsilon_3$, which passes through zero at f_{pe} and is negative below it.

Spherical. The roles are reversed: at $\theta = 90°$, $\varepsilon_{\mathrm{eff}}^{\mathrm{dir}} = \varepsilon_1$ (highest capacitance, highest $|Z|$); at $\theta = 0°$, $\varepsilon_{\mathrm{eff}}^{\mathrm{dir}} = \varepsilon_3$ (lowest capacitance). This reversal is confirmed by the capacitance tables: in Table 3 the maximum is always at $\theta = 0°$, whereas in Table 4 it is at $\theta = 90°$.

All angles converge above f_{uh} in both geometries, where $\varepsilon_1 \approx \varepsilon_3 \approx 1$ and the plasma contribution to the tensor is negligible.

6.4 Phase Behaviour and Capacitive/Inductive Transitions

The phase of Z cleanly maps the capacitive ($\angle Z \approx +90°$) and inductive ($\angle Z \approx -90°$) frequency regimes. In both geometries the device is capacitive above f_{uh} and transitions to inductive immediately below it. For Case 1, the separation of f_{pe} and f_{uh} creates a narrow inductive window between the two resonances, visible as two phase reversals in close succession. The collision frequency $\nu = 0.02\,\omega_{pe}$ prevents the phase from reaching the ideal $\pm 90°$ limits and rounds the transitions into smooth curves. Higher densities show sharper transitions because ν/ω_{uh} decreases as f_{pe} increases.

6.5 Geometry Comparison

The vacuum capacitances of the two geometries are nearly identical (1.605 pF vs. 1.669 pF), so differences in the plasma-filled impedance spectra are due to the anisotropy interaction alone. The cylindrical geometry samples a single well-defined radial direction, making the effective-permittivity approximation very accurate (the ε_2 Hall term is the only correction). The spherical geometry samples all orientations simultaneously; the averaged formula $\varepsilon_{\mathrm{eff}} = (2\varepsilon_1 + \varepsilon_3)/3$ is therefore a more

robust analytic reference than the directed formula, particularly at intermediate angles where the directed formula picks a single equatorial permittivity that may not represent the global average well.

7. Conclusion

A combined finite-element and analytic study of the RF impedance of plasma-filled cylindrical and spherical capacitors has been presented. The key findings are:

1. **FEA–analytic agreement.** The effective-permittivity analytic formulas agree with FEA results to within a few percent across most of the 1–30 MHz sweep for both geometries. The primary source of discrepancy is the neglect of the Hall term ε_2 at intermediate B_0 angles.
2. **Upper-hybrid resonance.** The dominant spectral feature in both geometries is a sharp impedance peak at f_{uh}. Its frequency scales as $\sqrt{f_{pe}^2 + f_{ce}^2}$, its Q-factor increases with density, and for $f_{pe} = 3\,\mathrm{MHz}$ it splits into two peaks (at f_{pe} and f_{uh}) due to the finite gap between the two resonant frequencies.
3. **Angle dependence and geometry reversal.** The B_0 orientation produces a strong angular spread in $|Z|$ at sub-resonance frequencies. The ordering of angles is reversed between the two geometries: $\theta = 0°$ gives the highest impedance in the cylindrical case while $\theta = 90°$ gives the highest in the spherical case, a direct consequence of the different projections of the permittivity tensor onto the radial field direction.
4. **Capacitance enhancement.** At 1 MHz the plasma-filled capacitances exceed the vacuum value by factors of 6–330× (cylindrical) and 4–139× (spherical) depending on density and angle, with the enhancement collapsing to unity above f_{uh}.
5. **Analytic formula accuracy.** For the cylindrical geometry the directed formula (Eq. 7) is accurate for all angles. For the spherical geometry the orientation-averaged formula (Eq. 9) is the more appropriate analytic reference because the spherical field geometry integrates the permittivity over all directions naturally.

Appendix: Simulation Parameters

Parameter	Value / Detail
Cylindrical $r_a/r_b/L$	5 mm / 20 mm / 40 mm
Spherical r_a/r_b	10 mm / 30 mm
Cylindrical C_{vac}	1.605 pF $\quad[\ln(r_b/r_a) = 1.386\,]$
Spherical C_{vac}	1.669 pF $\quad[\,4\pi\varepsilon_0 r_a r_b/(r_b - r_a)\,]$
B_0 magnitude	50 µT $\Rightarrow$ $\lvert f_{ce}\rvert = 1.40$ MHz
B_0 angles θ	$0°,\ 30°,\ 60°,\ 90°$ from symmetry axis
f_{pe} cases	3, 5, 8, 12 MHz
Collision frequency	$\nu = 0.02\,\omega_{pe}$ (electron only; stationary-ion model)
Ion species	Protons: $m_i = 1$ amu, $Z = 1$, $n_i = n_e$
Frequency sweep	40 log-spaced points, 1–30 MHz
Mesh $H_{\max}$	$(r_b - r_a)/3$
Phasor convention	$e^{+j\omega t} \Rightarrow \omega^* = \omega - j\nu$
Cylindrical charge method	`evaluateCGradient` at nodes retracted 5% inward; Delaunay triangulation area weights
Spherical charge method	Manual FE assembly; shape-function gradient evaluation; convex-hull triangulation area weights
MATLAB toolboxes	PDE Toolbox (`solvepde`, `evaluateCGradient`) for cylindrical; custom sparse FE solver for spherical

Complete simulation parameter reference for both geometries.

References

References

[1] Anthropic, "Claude Sonnet 4.6," Large language model, Anthropic, PBC, San Francisco, CA, USA. Accessed: Apr. 2025. [Online]. Available: https://www.anthropic.com

[2] OpenAI, "ChatGPT (GPT-4o)," Large language model, OpenAI, LP, San Francisco, CA, USA. Accessed: Apr. 2025. [Online]. Available: https://www.openai.com